Supplementary Material

Smallest Stable Si/SiO_2 Interface that Suppresses Quantum Tunneling from Machine-Learning based Global Search

Ye-Fei Li* and Zhi-Pan Liu*

Corresponding Author: yefeil@fudan.edu.cn; zpliu@fudan.edu.cn

Collaborative Innovation Center of Chemistry for Energy Material, Shanghai Key Laboratory of Molecular Catalysis and Innovative Materials, Key Laboratory of Computational Physical Science, Department of Chemistry, Fudan University, Shanghai 200433, China

Supplementary Methods

1. ML-interface Method

ML-interface contains three consecutive steps, OR screening, interface generation and global optimization. Below we elaborate the details of these steps.

1.1. OR Screening

OR screening step aims to identify the optimal OR of lattice-matched interfaces by using a modified PTMC. The PTMC takes the existence of invariant plane as the basic geometric constraint, where the lattice is neither stretched nor compressed during phase transition. The key step of PTMC is to compute the orientation of the invariant plane through the lattice correspondence. The basic idea of PTMC and corresponding mathematical methods can be adapted to predict the OR in heterojunctions, because the match of lattices is also a key requirement for a good interface. The major difference between the two application scenarios is that in martensitic transformation, the lattice correspondence is explicitly defined by the phase transition channel with the lowest barrier, while in heterojunction, any lattice correspondence is allowed since it is independent of any specific phase transition. Therefore, the basic idea to predict the OR of lattice-matched interfaces is to sample numerous lattice correspondences by changing the definition of the unit cell and then apply PTMC to calculate the orientation of invariant plane.

(a) Generate Lattice Correspondences

In phenomenological theory of martensitic crystallography (PTMC), the lattice correspondence is given by the deformation gradient **F** in Eq. (1).

$$\mathbf{TF} = \mathbf{M} \qquad (1)$$

where **T** and **M** are the lattice parameters of two crystals that compose an interface. Both **T** and **M** are (3×3) matrices, where each row represents a basis vector of the unit cell. Mathematically, the definition of lattice parameters is not unique, which can be represented by the product of the lattice parameters of primitive cell and a transformation matrix, as shown in Eq. (2)-(3).

$$\mathbf{T} = \mathbf{AT'} \qquad (2)$$

$$\mathbf{M} = \mathbf{BM'} \qquad (3)$$

T' and **M'** the lattice parameters of primitive cell for two crystals. **A** and **B** are the transformation matrices. All matrix elements of **A** and **B** are integers due to the translational symmetry of lattice. Any transformation matrices **A** and **B** with positive determinant are allowed. Therefore, we can generate numerous lattice correspondences by exhausting matrices **A** and **B**.

Because there is an infinite number of transformation matrices **A** and **B**, a cutoff must be applied. In our implementation, we set the matrix elements A_{ij} and $B_{ij} \in \{-2, -1, 0, 1, 2\}$, which is enough to

find all important ORs. Noted that our tests show that the simultaneous enumeration of both **A** and **B** matrices is necessary. Otherwise, some important OR might be missed.

(b) Calculate the Orientation of Invariant Plane

According to the polar decomposition, the deformation gradient **F** (see Eq. (1)) can be decomposed into rotation and stretching. The Cauchy-Green deformation tensor **C** is then constructed to eliminate the rotation in **F**.

$$\mathbf{C} = \mathbf{F}^{\mathbf{T}}\mathbf{F} \qquad (4)$$

Next, we perform an eigendecomposition of **C**:

$$\mathbf{C}\mathbf{e}_i = \mathrm{I}_i\mathbf{e}_i \quad (i=1,2,3) \qquad (5)$$

I_i and $\mathbf{e}_i$ are the eigenvalues and eigenvectors, which represent the magnitude and direction of strain during phase transition. For clarity, we sort the eigenvalues as $I_1 < I_2 < I_3$. According to PTMC, the existence of invariant plane requires $I_2 = 1$, $I_1 < 1$, and $I_3 > 1$.[1-3] Otherwise, no invariant plane exists for this lattice correspondence. Thus, we screen out the lattice correspondences that satisfy $0.95 < I_2 < 1.05$.

In these lattice correspondences, the vector $\mathbf{e}_2$ represents a strain invariant line (**sil**). Along **sil**, the lattice is neither stretched nor compressed during lattice transformation. The vector of another strain invariant line ($\mathbf{sil}_2$) is calculated by the linear combination of $\mathbf{e}_1$ and $\mathbf{e}_3$ through formulas (6)-(8):

$$a^2 + c^2 = 1 \qquad (6)$$

$$a^2 I_1 + c^2 I_3 = 1 \qquad (7)$$

$$\mathbf{sil}_2 = a\mathbf{e}_1 + c\mathbf{e}_3 \qquad (8)$$

where a and c are the coefficients of linear combination. The normal vector of strain invariant plane (**sip**) is then given by

$$\mathbf{sip} = \mathbf{e}_2 \times \mathbf{sil}_2 \qquad (9)$$

1.2. Interface Generation

(a) Calculate Miller indices and basis vectors of the invariant plane

The Miller indices of invariant plane can be determined from **sip** and **T**, as shown in Eq. (10).

$$\begin{pmatrix} h \\ k \\ l \end{pmatrix} = \mathbf{T}^{\mathbf{T}} \cdot \frac{\mathbf{sip}}{d_{hkl}} \qquad (10)$$

where $\mathbf{T}^{\mathbf{T}}$ is the transpose of lattice parameters **T**; (hkl) the Miller indices; d_{hkl} the d-spacing. However, this approach will produce high Miller indices, which has a large surface unit cell with a large number of atoms. Instead, we adopt the following approach to computing the approximate low Miller index of an invariant plane: (i) enumerate a series of low Miller indices {(h'k'l')} by setting h', k', l' ≤ 5; (ii) Calculate the normal vectors **n** for the trial Miller indices by using Eq. (11); (iii) determine the optimal low Miller indices that has the smallest angle between **n** and **sip**.

$$\frac{\mathbf{n}}{d_{h'k'l'}} = (\mathbf{T}^{\mathbf{T}})^{-1} \cdot \begin{pmatrix} h' \\ k' \\ l' \end{pmatrix} \qquad (11)$$

The Miller indices of the invariant plane of M are the same as that of **T**. That is, if the Miller indices of the invariant plane for lattice **T** is (101), then the corresponding Miller indices for lattice **M** is also (101).

Aside from the Miller indices, we need to further determine the basis vectors of the invariant plane. To build an interface with periodicity, the basis vectors of two phases must be matched. To this end, we use the Niggli reduction[4-7] to produce the matched basis vectors for both crystals.

(b) Generate Initial Guess for Interface Structures

In this section, we use a graph-based approach to automatically generate the atomic structures of interfaces. The flowchart of this approach is shown in Figure S1. We first reshape the new unit cell by the way that edges **a** and **b** are along with the basis vectors, while edge **c** is chosen so that it is shortest in periodicity. In the reshaped unit cell, (001) represents the invariant plane. Then we recognize the bonds by combining the criteria of covalent radii of elements[8] and the Voronoi partition.[9, 10] The covalent radii of elements are used to check whether two atoms bond together, and the Voronoi partition is adopted to delete unreasonable bonds in geometry. Our test shows that this approach can correctly produce the coordinate numbers for various crystals, such as TiO_2, GaP, SiO_2, Si, etc. If only covalent radii of elements are utilized, the coordinate number is usually overestimated and sensitive to the criteria of radii.

Next, we convert the crystal to a direct graph, so-called “network flow”. Specifically, we remove the bonds that cut through (001) plane, and convert the remaining structure to a graph, where the atoms correspond to the nodes and the bonds correspond to the edges. We then add a new edge for each terminal node (see red cycles in Figure S1b) to a virtual source or sink node (see purple cycles in Figure S2b). Finally, we convert the graph to a directed graph by setting the capacity of each edge: we set the capacity to infinity for the edges directly connected to the source or sink nodes; we set the capacity to 1 for both directions of other edges.

Subsequently, we cleave two slab models from bulk crystals by applying the max-flow min-cut theorem that calculates the way of cutting the fewest edges to separate a network flow in half.[11, 12] The max-flow min-cut theorem states that the maximum flow through any network from source to sink is exactly the sum of the edge capacities that, if removed, would disconnect the source from the sink. In other words, the max-flow from source to sink is equal to the min-cut necessary to separate source from sink. Flow can apply to anything, while in our case, it means the bond order in the crystal structures.

Next, we glue two slab models in a common unit cell by maximizing the number of bonds in the interface. Since the lattice match has been satisfied when generating the slab models, we can directly build an interface by gluing two slabs into a common unit cell. In this case, only the degree of translation freedom for the slabs remains, which greatly reduces the complexity to locate the stable structure of interface. To adjust the promising configuration between two slabs, we perform a series of rigid translations for the slabs and estimate the number of bonds at the interface. To correctly count the number of bonds, we again use the Voronoi partition to remove the unreasonable bonds in geometry. The interfacial structure with the largest number of bonds is chosen as the initial guess for global optimization.

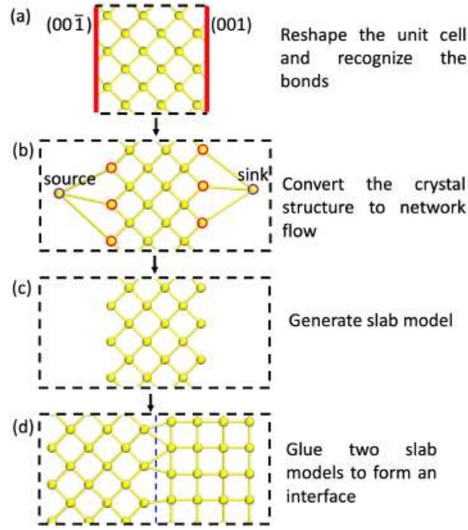

Figure S1. Flowchart for generating the atomic structures of interfaces. The red lines in (a) represent the invariant plane determined by PTMC; The purple cycles in (b) the source and sink nodes; The red cycles in (b) the terminal nodes; The blue dashed line in (d) the interface.

1.3. Global Optimization

To relax the interfacial atoms and explore possible reconstructions, SSW global optimization[13-15] is carried out to search for the stable interfacial structure. SSW algorithm can explore unbiasedly both minima and saddle points on PES with small step size in structure displacement. In SSW, an automated climbing mechanism is implemented to manipulate a structural configuration moving smoothly from a local minimum to a high-energy configuration along one random mode direction. In one particular SSW step, a modified PES is utilized for moving from the current minimum to a high energy configuration, in which a series of bias Gaussian potential is added one by one consecutively along the direction. Once the high energy configuration is reached, all bias potentials are removed and the local optimization is performed to quench the structure to a new minimum. At the end of the SSW step, the Metropolis Monte Carlo scheme is applied to accept/refuse the new minimum.

To speed up the SSW global optimization, a global neural network (NN) potential[16, 17] is utilized. The overall NN computational cost is roughly 10^3 to 10^4 times lower than that using Density Functional Theory (DFT) directly.[16, 17] The details of SSW and NN potential energy surface can be found in our previous literature.[13-17]

To search the nonstoichiometric Si/SiO_2 interfaces, we carried out a grand canonical Monte Carlo (GCMC) move after every 500 SSW-NN steps. In each GCMC move, we randomly add or remove an O/Si atom at the interface, and estimate the corresponding energy change. The probability of accepting the GCMC move (P) is calculated by Eq. (12)-(13)

$$P(N \rightarrow N+1) = \min[1, \frac{V}{\Lambda^3(N+1)}\exp\{\beta[\mu_{O/Si} - E(N+1) + E(N)]\}] \qquad (12)$$

$$P(N \rightarrow N-1) = \min[1, \frac{\Lambda^3 N}{V}\exp\{\beta[\mu_{O/Si} + E(N-1) - E(N)]\}] \quad (13)$$

where V is the accessible volume; $\Lambda = \sqrt{(h^2/2\pi m k_B T)}$ is the De Broglie thermal wavelength; $\mu_{O/Si}$ the chemical potential of O or Si, which is evaluated by Eq. (14)-(15).

$$\mu_{Si} = E_{Si} \quad (14)$$

$$\mu_O = (E_{SiO2} - E_{Si})/2 \quad (15)$$

E_{Si} is the DFT energy of bulk Si, while E_{SiO2} is the DFT energy of α-quartz, the most stable phase of SiO_2 polymorphs.

1.4. Computational Details

All DFT calculations were carried out within the periodic plane wave framework as implemented in Vienna ab initio simulation package (VASP).[18] The electron-ion interaction was represented by the projector augmented wave (PAW). The geometry optimization, interfacial energy, and the electronic structures are calculated by PBE functional. Since the PBE underestimates the bandgap, the electronic structures of all Si/SiO_2 interfaces are recomputed by hybrid HSE06 with the PBE geometry. The kinetic energy cutoffs of plane wave are set as 500 eV for variable-cell and 400 eV for single-point calculations. The k-point mesh utilized was up to (4 × 4 × 4) for bulk and (3 × 3 × 1) for heterojunctions in the Gamma centered grids, which is accurate enough for these systems. The geometry convergence criterion was set as 0.08 eV/Å for the maximal component of force and 0.08 GPa for stress. For each interface, we search at least 10^4 minima to ensure we identify the most stable structure.

The SSW-NN is carried out by the LASP software developed by our group.[19] The Si-Hf-O-H quaternary potential, a general potential for semiconductors interfaces, is utilized. The data sets for the training of potential are summarized in Table S2. The LASP software merges two major simulation tools (SSW global optimization and NN PES), and is now shaped toward a software platform for many purposes, including atomistic simulation, PES data building and exchange, and even for global NN potential generation. A large set of powerful simulation techniques has been assembled into LASP program (www.lasphub.com) to simplify the usage and to enlarge the scope of the current atomistic simulation.

The interfacial energy of Si/SiO_2 heterojunction is calculated by Eq. (16).

$$\gamma = (E_{Si/SiO2} - E_{Si} - E_{SiO2} - n_O \times \mu_O - n_{Si} \times \mu_{Si})/2A \quad (16)$$

The denominator A is the interfacial area in periodicity. $E_{Si/SiO2}$, E_{Si}, and E_{SiO2} are DFT energies for Si/SiO_2 interface, bulk Si, and bulk SiO_2, respectively. The term n_O and n_{Si} are the numbers of O and Si atoms added by GCMC move.

2. Transfer-Matrix Method

The transfer-matrix method is based on the band theory, which assumes that the electrons travel in a static potential without dynamically interacting with lattice vibrations, other electrons, etc. This method approximates the potential energy surface by a stepwise potential profile characterized by sequential potential energy U_i. The solutions of the Schrodinger equation for each step are given by

$$\psi_i(x) = A_i e^{ik_i x} + B_i e^{-ik_i x} \quad (17)$$

$$\psi_{i+1}(x) = A_{i+1} e^{ik_{i+1} x} + B_{i+1} e^{-ik_{i+1} x} \quad (18)$$

where $k_i = \frac{1}{\hbar}\sqrt{2m^*(E - U_i)}$ is the wave vector; m^* is the carrier effective mass; ħ is the reduced Planck constant; E is the energy relative to Fermi level. Due to the continuity of $\psi_i(x)$ and $d\psi_i(x)/dx$ at each boundary, the amplitudes A_i and B_i are corrected with A_{i+1} and B_{i+1} as

$$\begin{bmatrix} A_i \\ B_i \end{bmatrix} = M_i \begin{bmatrix} A_{i+1} \\ B_{i+1} \end{bmatrix} \quad (19)$$

The transfer matrix M_i is given by

$$M_{11} = \frac{1}{2}\left(1 + \frac{m_i^*}{m_{i+1}^*}\frac{k_{i+1}}{k_i}\right)e^{-ik_i L_i}$$

$$M_{12} = \frac{1}{2}\left(1 - \frac{m_i^*}{m_{i+1}^*}\frac{k_{i+1}}{k_i}\right)e^{-ik_i L_i} \quad (20)$$

$$M_{21} = \frac{1}{2}\left(1 - \frac{m_i^*}{m_{i+1}^*}\frac{k_{i+1}}{k_i}\right)e^{ik_i L_i}$$

$$M_{22} = \frac{1}{2}\left(1 + \frac{m_i^*}{m_{i+1}^*}\frac{k_{i+1}}{k_i}\right)e^{ik_i L_i}$$

L_i is the length of one step potential. The total transfer matrix is calculated by multiplying transfer matrix of each step region, as

$$M = \prod_{i=1}^{i=N} M_i \quad (21)$$

The transformation coefficient T is then

$$T = \frac{m_0^*}{m_N^*}\frac{k_N}{k_0}\left(\frac{1}{M_{11}}\right)^2 \quad (22)$$

T represents the probability of carrier tunneling through a potential barrier.

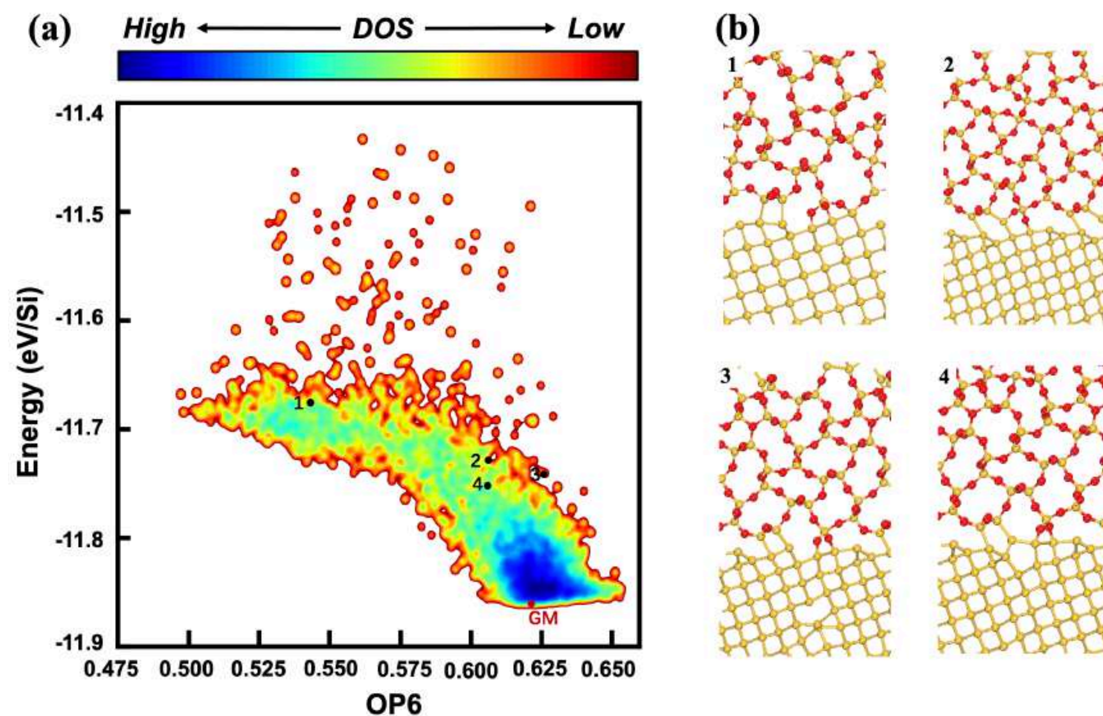

Figure S2. Global potential energy surface contour plot for Si/SiO_2 interface on Si(210) using minima from ML-interface. The y axis is the energy per Si. GM: global minimum. OP6: the structure order parameter with l = 6. Some representative amorphous interfaces are labeled by dots in Figure (a) and their structures are plotted in Figure (b).

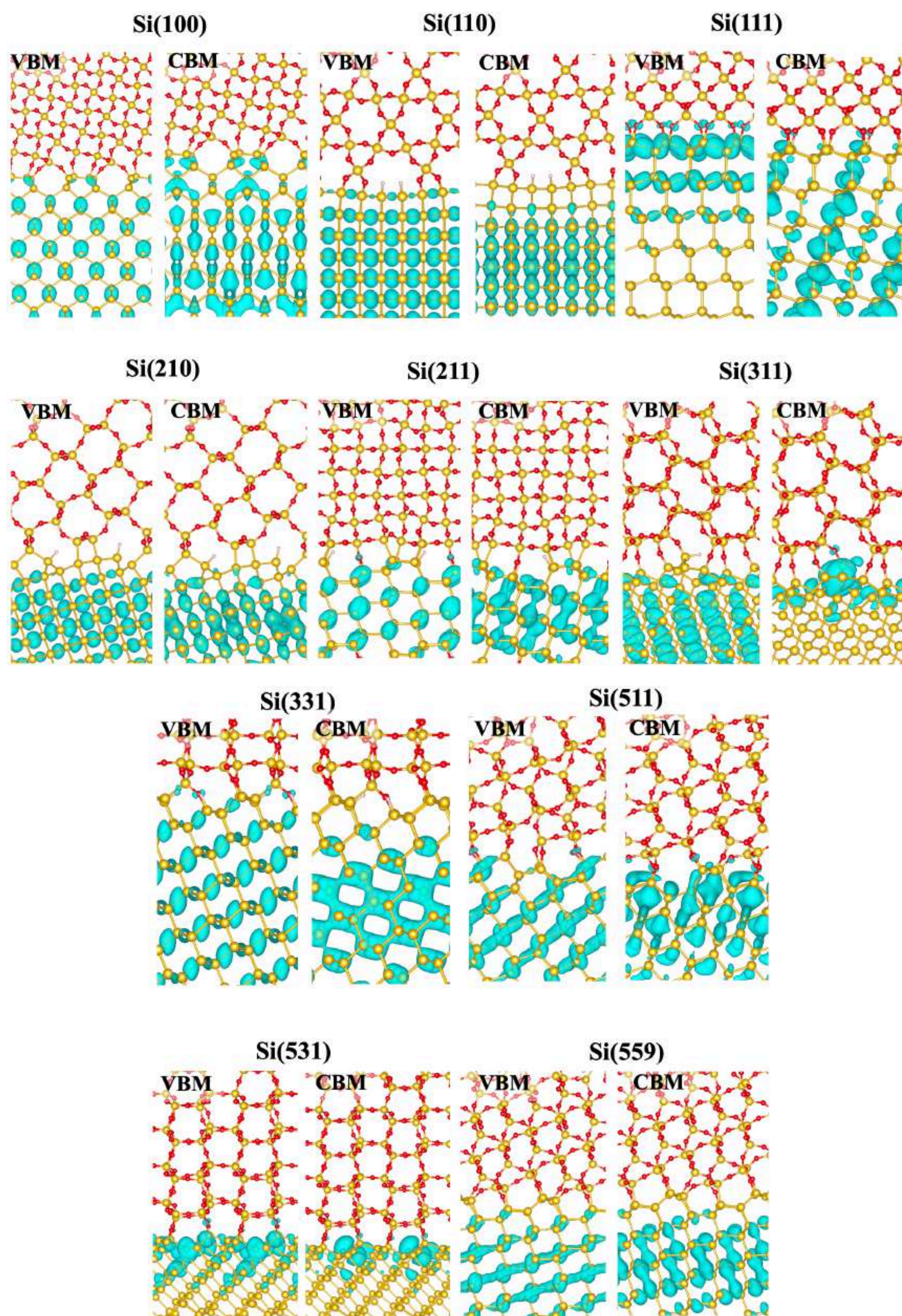

Figure S3. Partial charge densities of VBM and CBM for 10 Si/SiO_2 interfaces calculated using HSE06.

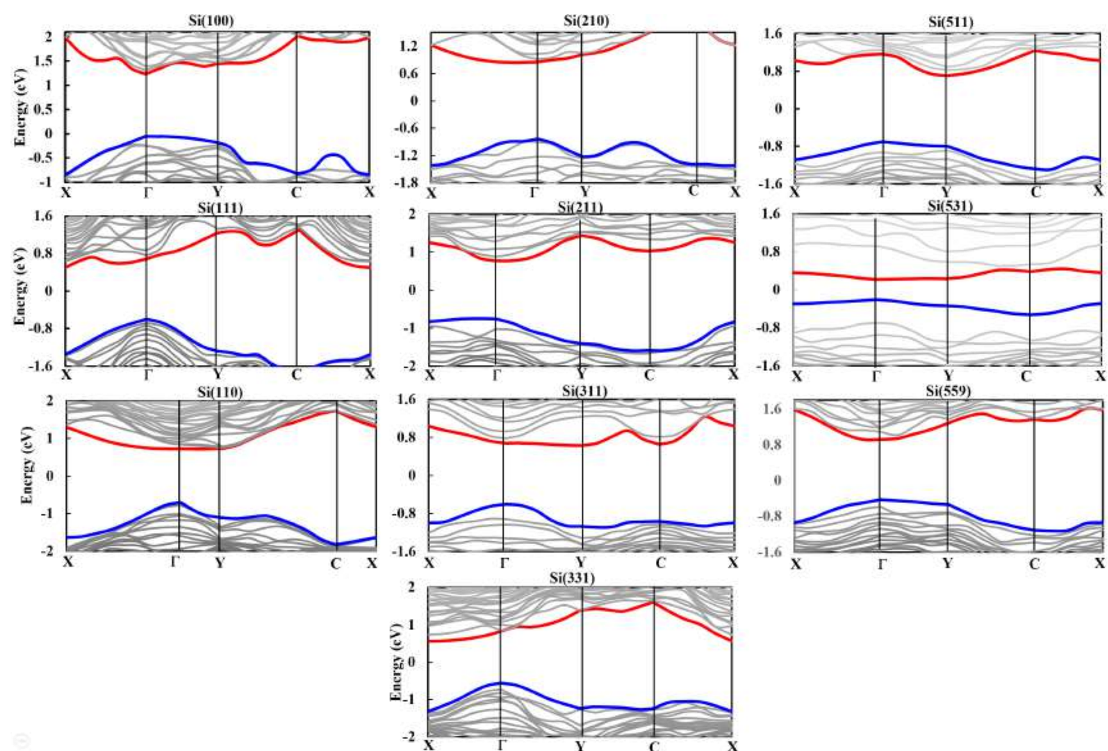

Figure S4. Band structures of 10 Si/SiO_2 interface using HSE06. The Blue lines represent the highest valence band and red lines represent the lowest conduction band. The coordinates of points in k path are Γ (0, 0, 0); X (0.5, 0, 0); Y (0, 0.5. 0); C (0.5, 0.5, 0).

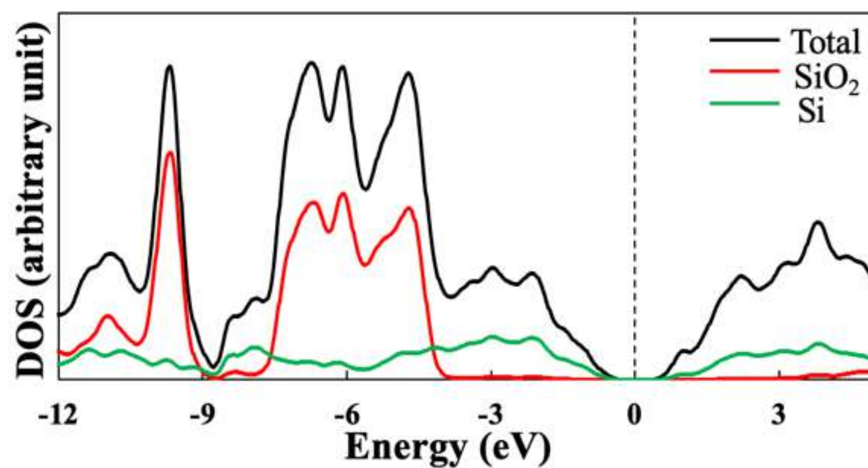

Figure S5. Density of states for $(100)_{Si}//(111)_{\alpha\text{-cristobalite}}$ interface using HSE06.

Figure S6. Partial charge densities of VBM and CBM for 10 Si/SiO2 interfaces using PBE functional.

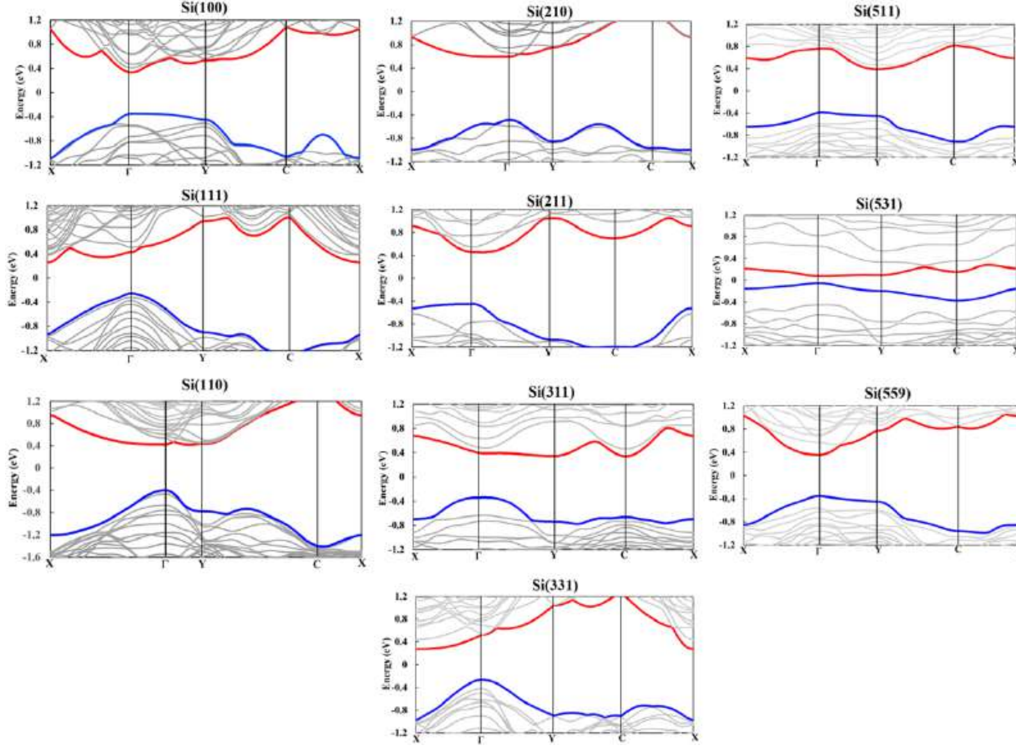

Figure S7. Band structures of 10 Si/SiO_2 interfaces using PBE functional. The Blue lines represent the highest valence band and red lines represent the lowest conduction band. The coordinates of points in k path are Γ (0, 0, 0); X (0.5, 0, 0); Y (0, 0.5. 0); C (0.5, 0.5, 0).

Table S1. Interface energies of Si/SiO_2 in this and previous works

this work		previous work	
Orientation	γ($J.m^{-2}$)	Orientation	γ($J.m^{-2}$)
Low-index Si/SiO_2 interface			
$(100)_{Si}//(111)_{\alpha\text{-crist}}$	0.93	Si(100)/α-quartz	0.99[a]
$(111)_{Si}//(110)_{\alpha\text{-crist}}$	1.13	Si(111)/a-SiO_2[d]	1.15[b]
$(110)_{Si}//(100)_{\alpha\text{-quartz}}$	1.27	Si(110)/α-quartz	1.83[c]
High-index Si/SiO_2 interface			
$(531)_{Si}//(010)_{\beta\text{-tridymite}}$	1.01	a-SiO_2/Si(331)	1.50[b]
$(210)_{Si}//(102)_{\beta\text{-tridymite}}$	1.16	a-SiO_2/Si(310)	1.66[b]
$(211)_{Si}//(1\bar{1}2)_{\alpha\text{-crist}}$	1.17	a-SiO_2/Si(410)	1.72[b]
$(511)_{Si}///(21\bar{1})_{\alpha\text{-quartz}}$	1.20	-	-
$(311)_{Si}//(1\bar{2}0)_{\beta\text{-tridymite}}$	1.23	-	-
$(559)_{Si}//(121)_{\alpha\text{-quartz}}$	1.27	-	-
$(331)_{Si}//(010)_{\alpha\text{-crist}}$	1.40	-	-

[a] recalculate using PBE with the interface proposed in PRL, 84 (2000), 943

[b] data from J. Appl. Phys., 119, (2016), 054103 using PBE.

[c] data from Phys. Rev. B, 73, (2006), 165312 using PW91.

[d] a-SiO_2 represents the amorphous-SiO_2.

Table S2. Carrier effective mass for 10 Si/SiO_2 interfaces using HSE06

OR	direction	m_h^* (m_e)	direction	m_h^* (m_e)	direction	m_e^* (m_e)	direction	m_e^* (m_e)
$(100)_{Si}//(111)_{\alpha\text{-cristobalite}}$	Γ→X	0.20	Γ→Y	**8.58**	Γ→X	**0.23**	Γ→Y	0.22
$(111)_{Si}//(110)_{\alpha\text{-cristobalite}}$	Γ→X	0.24	Γ→Y	**0.38**	X→Γ	0.17	X→C	**0.94**
$(110)_{Si}//(100)_{\alpha\text{-quartz}}$	Γ→X	**0.32**	Γ→Y	0.12	Γ→X	**16.89**	Γ→Y	0.11
$(531)_{Si}//(010)_{\beta\text{-tridymite}}$	Γ→X	**1.14**	Γ→Y	0.84	Γ→X	0.95	Γ→Y	**4.90**
$(210)_{Si}//(102)_{\beta\text{-tridymite}}$	Γ→X	**0.48**	Γ→Y	0.31	Γ→X	**6.76**	Γ→Y	0.25
$(211)_{Si}//(1\bar{1}2)_{\alpha\text{-cristobalite}}$	Γ→X	**6.53**	Γ→Y	0.22	Γ→X	0.32	Γ→Y	**0.63**
$(511)_{Si}///(21\bar{1})_{\alpha\text{-quartz}}$	Γ→X	0.36	Γ→Y	**0.71**	Y→C	**0.73**	Y→Γ	0.66
$(311)_{Si}//(1\bar{2}0)_{\beta\text{-tridymite}}$	Γ→X	**1.07**	Γ→Y	0.62	Y→C	0.44	Y→Γ	**3.12**
$(559)_{Si}//(121)_{\alpha\text{-quartz}}$	Γ→X	0.35	Γ→Y	**0.46**	Γ→X	0.76	Γ→Y	**1.05**
$(331)_{Si}//(010)_{\alpha\text{-cristobalite}}$	Γ→X	0.31	Γ→Y	**0.42**	X→Γ	**3.56**	X→C	0.14

† The bold numbers indicate the heavier effective mass between two directions.

Table S3. Carrier effective mass for 10 Si/SiO_2 interfaces using PBE

OR	direction	m_h^* (m_e)	direction	m_h^* (m_e)	direction	m_e^* (m_e)	direction	m_e^* (m_e)
$(100)_{Si}//(111)_{\alpha\text{-cristobalite}}$	Γ→X	0.16	Γ→Y	**13.41**†	Γ→X	**0.22**	Γ→Y	0.19
$(111)_{Si}//(110)_{\alpha\text{-cristobalite}}$	Γ→X	0.25	Γ→Y	**0.42**	X→Γ	0.18	X→C	**0.97**
$(110)_{Si}//(100)_{\alpha\text{-quartz}}$	Γ→X	**0.26**	Γ→Y	0.11	Γ→X	**13.15**	Γ→Y	0.40
$(531)_{Si}//(010)_{\beta\text{-tridymite}}$	Γ→X	**0.73**	Γ→Y	0.56	Γ→X	0.81	Γ→Y	**4.02**
$(210)_{Si}//(102)_{\beta\text{-tridymite}}$	Γ→X	**0.52**	Γ→Y	0.31	Γ→X	**9.58**	Γ→Y	0.21
$(211)_{Si}//(1\bar{1}2)_{\alpha\text{-cristobalite}}$	Γ→X	**7.31**	Γ→Y	0.19	Γ→X	0.36	Γ→Y	**0.66**
$(511)_{Si}///(21\bar{1})_{\alpha\text{-quartz}}$	Γ→X	0.25	Γ→Y	**0.85**	Y→C	**0.71**	Y→Γ	0.58
$(311)_{Si}//(1\bar{2}0)_{\beta\text{-tridymite}}$	Γ→X	**3.11**	Γ→Y	0.70	Y→C	0.20	Y→Γ	**2.49**
$(559)_{Si}//(121)_{\alpha\text{-quartz}}$	Γ→X	0.30	Γ→Y	**0.48**	Γ→X	**0.78**	Γ→Y	0.30
$(331)_{Si}//(010)_{\alpha\text{-cristobalite}}$	Γ→X	0.23	Γ→Y	**0.40**	X→Γ	**3.94**	X→C	0.13

† The bold numbers indicate the heavier effective mass between two directions.

Table S4. Data sets for the Si-Hf-O-H potential

Species	N_{atom}	cluster	layer	bulk	total
Si14	14	0	0	8	8
Si15	15	125	0	15	140
Si16	16	781	93	2921	3795
Si17	17	0	5	6	11
Si30	30	0	0	5	5
Si31	31	0	0	6	6
Si32	32	0	0	27	27
O1-Si2-Hf10	13	0	1	12	13
O1-Si3-Hf9	13	0	1	7	8
O1-Si4-Hf8	13	0	1	7	8
O1-Si5-Hf7	13	0	3	14	17

O1-Si6-Hf6	13	0	4	13	17
O1-Si7-Hf5	13	0	10	25	35
O1-Si8-Hf4	13	0	0	11	11
O1-Si9-Hf3	13	0	1	19	20
O1-Si10-Hf2	13	0	14	19	33
O1-Si11-Hf1	13	0	5	25	30
O2-Hf10	12	0	1	11	12
O2-Si3-Hf7	12	0	3	11	14
O2-Si4-Hf4	10	0	0	11	11
O2-Si4-Hf6	12	0	1	7	8
O2-Si5-Hf3	10	0	5	7	12
O2-Si5-Hf5	12	0	0	1	1
O2-Si7-Hf3	12	0	0	1	1
O2-Si8-Hf2	12	0	2	13	15
O2-Si9-Hf1	12	0	1	2	3
O3-Si5-Hf13	21	0	3	8	11
O3-Si8-Hf10	21	0	1	6	7
O3-Si10-Hf8	21	0	8	1	9
O3-Si12-Hf6	21	0	2	5	7
O3-Si14-Hf4	21	0	4	14	18
O3-Si15-Hf3	21	0	6	8	14
O3-Si17-Hf1	21	0	1	5	6
O4-Si1-Hf3	8	0	0	13	13
O4-Si2-Hf2	8	0	0	10	10
O4-Si2-Hf6	12	0	4	13	17
O4-Si3-Hf1	8	0	0	10	10
O4-Si3-Hf5	12	0	4	7	11
O4-Si4-Hf4	12	0	0	1	1
O4-Si5-Hf3	12	0	0	7	7
O4-Si6-Hf2	12	0	0	3	3
O4-Si7-Hf1	12	0	0	21	21
O4-Si8-Hf14	26	0	2	7	9
O4-Si8-Hf40	52	0	3	6	9
O4-Si12-Hf36	52	0	2	6	8
O4-Si16-Hf32	52	0	2	5	7
O4-Si20-Hf28	52	0	13	15	28
O4-Si24-Hf24	52	0	7	9	16
O4-Si28-Hf20	52	0	11	25	36
O4-Si32-Hf16	52	0	2	5	7
O4-Si36-Hf12	52	0	12	16	28
O4-Si40-Hf8	52	0	8	32	40

O4-Si44-Hf4	52	0	10	7	17
O5-Si11-Hf16	32	0	4	6	10
O6-Si1-Hf7	14	0	0	3	3
O6-Si2-Hf6	14	0	0	6	6
O6-Si3-Hf5	14	0	1	7	8
O6-Si4-Hf4	14	0	0	3	3
O6-Si5-Hf3	14	0	0	8	8
O6-Si5-Hf10	21	0	2	7	9
O6-Si6-Hf2	14	0	0	8	8
O6-Si6-Hf9	21	0	6	8	14
O6-Si7-Hf1	14	0	0	2	2
O6-Si7-Hf8	21	0	3	3	6
O6-Si7-Hf11	24	0	1	9	10
O6-Si8-Hf7	21	0	3	20	23
O6-Si9-Hf6	21	0	2	4	6
O6-Si10-Hf8	24	0	0	5	5
O6-Si10-Hf26	42	0	0	7	7
O6-Si11-Hf4	21	0	4	10	14
O6-Si12-Hf6	24	0	0	2	2
O6-Si13-Hf2	21	0	3	4	7
O6-Si13-Hf5	24	0	5	4	9
O6-Si14-Hf4	24	0	0	1	1
O6-Si16-Hf20	42	0	0	5	5
O6-Si20-Hf16	42	0	0	9	9
O6-Si24-Hf12	42	0	0	3	3
O6-Si28-Hf8	42	0	1	21	22
O6-Si30-Hf6	42	0	0	26	26
O8-Hf4	12	0	54	336	390
O8-Si1-Hf3	12	0	44	166	210
O8-Si2-Hf2	12	0	78	269	347
O8-Si2-Hf6	16	0	13	10	23
O8-Si3-Hf1	12	0	117	325	442
O8-Si4-Hf4	16	0	0	1	1
O8-Si4-Hf11	23	0	11	16	27
O8-Si5-Hf3	16	0	0	2	2
O8-Si6-Hf2	16	0	1	9	10
O8-Si7-Hf1	16	0	3	7	10
O8-Si9-Hf6	23	0	0	9	9
O8-Si11-Hf4	23	0	3	3	6
O8-Si12-Hf3	23	0	2	4	6
O8-Si12-Hf28	48	0	11	10	21

O8-Si13-Hf2	23	0	5	8	13
O8-Si16-Hf16	40	0	4	6	10
O8-Si16-Hf24	48	0	0	7	7
O8-Si16-Hf28	52	0	0	2	2
O8-Si20-Hf12	40	0	3	2	5
O8-Si20-Hf20	48	0	0	10	10
O8-Si32-Hf8	48	0	14	16	30
O8-Si36-Hf4	48	0	1	9	10
O10-Si1-Hf7	18	0	0	4	4
O10-Si3-Hf5	18	0	0	4	4
O10-Si4-Hf4	18	0	4	15	19
O10-Si5-Hf3	18	0	0	3	3
O10-Si5-Hf17	32	0	0	3	3
O10-Si6-Hf2	18	0	4	29	33
O10-Si7-Hf1	18	0	5	5	10
O10-Si7-Hf15	32	0	1	6	7
O10-Si8-Hf14	32	0	2	5	7
O10-Si14-Hf8	32	0	1	5	6
O10-Si15-Hf7	32	0	0	3	3
O10-Si21-Hf1	32	0	0	10	10
O10-Si22-Hf32	64	0	0	20	20
O12-Hf6	18	0	49	191	240
O12-Si1-Hf5	18	0	64	200	264
O12-Si2-Hf4	18	0	27	166	193
O12-Si3-Hf3	18	0	45	184	229
O12-Si3-Hf5	20	0	5	25	30
O12-Si4-Hf2	18	0	44	154	198
O12-Si4-Hf4	20	0	9	6	15
O12-Si5-Hf1	18	0	56	211	267
O12-Si5-Hf3	20	0	6	18	24
O12-Si6	18	0	1429	11804	13233
O12-Si6-Hf2	20	0	7	12	19
O12-Si7-Hf1	20	0	5	15	20
O12-Si10-Hf20	42	0	0	17	17
O12-Si12-Hf18	42	0	0	5	5
O12-Si14-Hf16	42	0	1	10	11
O12-Si16-Hf14	42	0	0	15	15
O12-Si18-Hf12	42	0	0	4	4
O12-Si20-Hf16	48	0	0	6	6
O12-Si20-Hf52	84	0	5	0	5
O12-Si22-Hf8	42	0	1	1	2

O12-Si26-Hf4	42	0	0	3	3
O12-Si32-Hf40	84	0	7	0	7
O12-Si40-Hf32	84	0	2	0	2
O12-Si48-Hf24	84	0	9	0	9
O12-Si56-Hf16	84	0	5	0	5
O12-Si60-Hf12	84	0	26	0	26
O12-Si68-Hf4	84	0	2	0	2
O13-Si4-Hf3	20	0	6	5	11
O14-Si6-Hf2	22	0	1	4	5
O14-Si7-Hf1	22	0	3	11	14
O15-Si2-Hf7	24	0	2	4	6
O15-Si3-Hf6	24	0	0	3	3
O15-Si5-Hf4	24	0	2	5	7
O15-Si6-Hf3	24	0	0	10	10
O15-Si7-Hf2	24	0	6	9	15
O15-Si8-Hf1	24	0	3	14	17
O16-Si1-Hf7	24	0	2	2	4
O16-Si3-Hf5	24	0	1	3	4
O16-Si4-Hf12	32	0	8	19	27
O16-Si5-Hf3	24	0	1	6	7
O16-Si6-Hf2	24	0	0	3	3
O16-Si7-Hf1	24	0	31	32	63
O16-Si8-Hf22	46	0	0	8	8
O16-Si8-Hf24	48	0	0	5	5
O16-Si12-Hf4	32	0	10	19	29
O16-Si12-Hf20	48	0	0	5	5
O16-Si16-Hf16	48	0	0	5	5
O16-Si20-Hf12	48	0	0	7	7
O16-Si24-Hf6	46	0	0	6	6
O16-Si24-Hf8	48	0	2	9	11
O16-Si28-Hf4	48	0	21	11	32
O16-Si32-Hf56	104	0	8	0	8
O18-Si2-Hf10	30	0	1	2	3
O18-Si4-Hf8	30	0	4	6	10
O18-Si6-Hf6	30	0	6	3	9
O18-Si7-Hf5	30	0	6	5	11
O18-Si8-Hf4	30	0	2	10	12
O18-Si9-Hf3	30	0	6	4	10
O18-Si10-Hf2	30	0	4	11	15
O18-Si11-Hf1	30	0	14	7	21
O19-Si8-Hf2	29	0	1	2	3

O20-Hf10	30	0	3	5	8
O20-Si1-Hf9	30	0	0	6	6
O20-Si2-Hf8	30	0	0	1	1
O20-Si3-Hf7	30	0	6	4	10
O20-Si4-Hf6	30	0	0	4	4
O20-Si7-Hf3	30	0	2	4	6
O20-Si8-Hf2	30	0	9	8	17
O20-Si9-Hf1	30	0	15	19	34
O20-Si10	30	0	1	309	310
O20-Si10-Hf34	64	0	0	5	5
O20-Si14-Hf30	64	0	0	8	8
O20-Si28-Hf16	64	0	0	3	3
O20-Si42-Hf2	64	0	0	23	23
O22-Hf11	33	0	1	2	3
O22-Si1-Hf10	33	0	0	2	2
O22-Si2-Hf9	33	0	4	4	8
O22-Si3-Hf8	33	0	0	1	1
O22-Si4-Hf7	33	0	0	5	5
O22-Si5-Hf6	33	0	0	1	1
O22-Si6-Hf5	33	0	0	3	3
O22-Si7-Hf4	33	0	0	1	1
O22-Si8-Hf3	33	0	0	5	5
O22-Si9-Hf2	33	0	0	3	3
O22-Si10-Hf1	33	0	0	2	2
O22-Si11	33	0	10	322	332
O24-Hf12	36	0	0	1	1
O24-Si1-Hf11	36	0	0	5	5
O24-Si2-Hf10	36	0	0	2	2
O24-Si3-Hf9	36	0	0	3	3
O24-Si4-Hf8	36	0	4	3	7
O24-Si4-Hf28	56	0	3	0	3
O24-Si5-Hf7	36	0	0	2	2
O24-Si6-Hf6	36	0	0	1	1
O24-Si7-Hf5	36	0	0	1	1
O24-Si8-Hf24	56	0	4	8	12
O24-Si9-Hf3	36	0	0	2	2
O24-Si10-Hf2	36	0	0	3	3
O24-Si11-Hf1	36	0	0	2	2
O24-Si12	36	0	0	303	303
O24-Si12-Hf20	56	0	3	15	18
O24-Si16-Hf16	56	0	7	0	7

O24-Si20-Hf12	56	0	15	3	18
O24-Si20-Hf40	84	0	4	0	4
O24-Si24-Hf8	56	0	3	6	9
O24-Si24-Hf36	84	0	14	0	14
O24-Si28-Hf4	56	0	0	8	8
O24-Si28-Hf32	84	0	2	0	2
O24-Si28-Hf44	96	0	7	0	7
O24-Si32-Hf28	84	0	23	0	23
O24-Si36-Hf24	84	0	6	0	6
O24-Si40-Hf32	96	0	4	0	4
O24-Si44-Hf16	84	0	7	0	7
O24-Si52-Hf8	84	0	1	0	1
O24-Si52-Hf20	96	0	14	0	14
O24-Si56-Hf16	96	0	2	0	2
O28-Si14-Hf2	44	0	6	8	14
O30-Si4-Hf14	48	0	0	6	6
O30-Si6-Hf12	48	0	0	3	3
O30-Si12-Hf6	48	0	0	8	8
O30-Si14-Hf4	48	0	7	1	8
O30-Si16-Hf2	48	0	3	9	12
O32-Si4-Hf12	48	0	140	163	303
O32-Si6-Hf10	48	0	0	1	1
O32-Si8-Hf8	48	0	236	225	461
O32-Si8-Hf24	64	0	6	10	16
O32-Si10-Hf6	48	0	0	1	1
O32-Si12-Hf4	48	0	242	338	580
O32-Si14-Hf2	48	0	0	38	38
O32-Si16-Hf44	92	0	22	0	22
O32-Si24-Hf8	64	0	4	31	35
O32-Si28-Hf4	64	0	8	11	19
O32-Si36-Hf24	92	0	9	0	9
O32-Si44-Hf16	92	0	3	0	3
O32-Si52-Hf8	92	0	3	0	3
O36-Si12-Hf12	60	0	0	1	1
O36-Si16-Hf8	60	0	0	2	2
O36-Si18-Hf6	60	0	0	1	1
O36-Si20-Hf4	60	0	0	3	3
O40-Hf20	60	0	0	2	2
O40-Si4-Hf28	72	0	6	9	15
O40-Si6-Hf14	60	0	0	12	12
O40-Si8-Hf12	60	0	0	4	4

O40-Si12-Hf20	72	0	4	0	4
O40-Si14-Hf6	60	0	0	27	27
O40-Si16-Hf4	60	0	0	14	14
O40-Si16-Hf16	72	0	17	26	43
O40-Si18-Hf2	60	0	3	24	27
O40-Si20	60	0	0	4	4
O40-Si20-Hf68	128	0	8	0	8
O40-Si24-Hf8	72	0	18	21	39
O40-Si28-Hf4	72	0	0	2	2
O40-Si28-Hf60	128	0	10	0	10
O40-Si32-Hf56	128	0	6	0	6
O40-Si56-Hf32	128	0	8	2	10
O44-Si2-Hf20	66	0	0	4	4
O44-Si4-Hf18	66	0	0	4	4
O44-Si12-Hf10	66	0	0	4	4
O44-Si16-Hf6	66	0	0	9	9
O44-Si22	66	0	0	5	5
O48-Hf24	72	0	129	176	305
O48-Si4-Hf20	72	0	103	246	349
O48-Si6-Hf18	72	0	0	7	7
O48-Si8-Hf16	72	0	106	107	213
O48-Si12-Hf12	72	0	107	127	234
O48-Si12-Hf20	80	0	22	43	65
O48-Si16-Hf8	72	0	99	186	285
O48-Si16-Hf16	80	0	29	57	86
O48-Si18-Hf6	72	0	0	2	2
O48-Si20-Hf4	72	0	156	213	369
O48-Si20-Hf12	80	0	7	9	16
O48-Si24	72	0	170	209	379
O48-Si24-Hf8	80	0	18	7	25
O48-Si28-Hf4	80	0	19	8	27
O52-Si16-Hf12	80	0	6	8	14
O56-Si28-Hf4	88	0	11	0	11
O60-Si8-Hf28	96	0	2	0	2
O60-Si20-Hf16	96	0	7	0	7
O60-Si24-Hf12	96	0	13	0	13
O60-Si28-Hf8	96	0	7	0	7
O60-Si32-Hf4	96	0	5	0	5
O63-Si28-Hf4	95	0	3	5	8
O64-Si4-Hf28	96	0	2	0	2
O64-Si23-Hf9	96	0	0	2	2

O64-Si24-Hf8	96	0	3	0	3
O64-Si27-Hf5	96	0	12	30	42
O64-Si28-Hf4	96	0	57	0	57
O64-Si30-Hf2	96	0	18	34	52
O72-Si16-Hf32	120	0	17	0	17
O72-Si24-Hf24	120	0	1	0	1
O72-Si32-Hf16	120	0	8	0	8
O72-Si40-Hf8	120	0	11	0	11
O72-Si44-Hf4	120	0	4	1	5
O80-Si4-Hf36	120	0	1	0	1
O80-Si12-Hf28	120	0	5	0	5
O80-Si16-Hf24	120	0	7	0	7
O80-Si28-Hf12	120	0	2	0	2
O80-Si32-Hf8	120	0	9	0	9
O80-Si36-Hf4	120	0	40	0	40
O80-Si40	120	0	1	0	1
O88-Si8-Hf36	132	0	5	0	5
O88-Si12-Hf32	132	0	6	0	6
O88-Si16-Hf28	132	0	2	0	2
O88-Si24-Hf20	132	0	2	0	2
O88-Si40-Hf4	132	0	5	0	5
O88-Si44	132	0	7	0	7
O96-Hf48	144	0	6	0	6
O96-Si12-Hf36	144	0	4	0	4
O96-Si16-Hf32	144	0	7	0	7
O96-Si48	144	0	3	0	3
H6-O19-Si4-Hf4	33	0	0	1	1
H6-O19-Si5-Hf3	33	0	0	1	1
H6-O19-Si6-Hf2	33	0	1	0	1
H6-O19-Si7-Hf1	33	0	0	1	1
H6-O19-Si8	33	0	36	30	66
H8-O28-Hf12	48	0	17	34	51
H8-O28-Si1-Hf11	48	0	19	41	60
H8-O28-Si2-Hf10	48	0	14	19	33
H8-O28-Si3-Hf9	48	0	7	13	20
H8-O28-Si4-Hf8	48	0	6	18	24
H8-O28-Si5-Hf7	48	0	11	16	27
H8-O28-Si6-Hf6	48	0	7	16	23
H8-O28-Si7-Hf5	48	0	10	17	27
H8-O28-Si8-Hf4	48	0	14	24	38
H8-O28-Si9-Hf3	48	0	18	42	60

H8-O28-Si10-Hf2	48	0	8	42	50
H8-O28-Si11-Hf1	48	0	21	65	86
H8-O28-Si12	48	0	1213	1127	2340
H10-O21-Hf8	39	0	1	0	1
H10-O21-Si1-Hf7	39	0	1	0	1
H10-O21-Si2-Hf6	39	0	1	0	1
H10-O21-Si7-Hf1	39	0	1	0	1
H10-O21-Si8	39	0	41	6	47
H12-O38-Si12-Hf4	66	0	1	6	7
H16-O56-Hf24	96	0	19	1	20
H16-O56-Si2-Hf22	96	0	5	0	5
H16-O56-Si4-Hf20	96	0	13	0	13
H16-O56-Si6-Hf18	96	0	2	0	2
H16-O56-Si8-Hf16	96	0	4	0	4
H16-O56-Si10-Hf14	96	0	21	0	21
H16-O56-Si12-Hf12	96	0	6	0	6
H16-O56-Si14-Hf10	96	0	40	15	55
H16-O56-Si16-Hf8	96	0	17	2	19
H16-O56-Si18-Hf6	96	0	23	6	29
H16-O56-Si20-Hf4	96	0	20	1	21
H16-O56-Si22-Hf2	96	0	35	1	36
H16-O56-Si24	96	0	5	0	5
H20-O42-Hf16	78	0	0	3	3
H24-O76-Si16-Hf16	132	0	2	0	2
H24-O76-Si24-Hf8	132	0	0	1	1
H26-O37-Hf12	75	0	0	36	36
H26-O37-Si1-Hf11	75	0	5	17	22
H26-O37-Si2-Hf10	75	0	23	13	36
H26-O37-Si3-Hf9	75	0	15	27	42
H26-O37-Si4-Hf8	75	0	8	7	15
H26-O37-Si5-Hf7	75	0	13	12	25
H26-O37-Si6-Hf6	75	0	3	9	12
H26-O37-Si7-Hf5	75	0	37	15	52
H26-O37-Si8-Hf4	75	0	19	26	45
H26-O37-Si9-Hf3	75	0	15	28	43
H26-O37-Si10-Hf2	75	0	52	26	78
H26-O37-Si11-Hf1	75	0	27	44	71
H26-O37-Si12	75	0	220	1120	1340
H40-O84-Si4-Hf28	156	0	3	0	3
total	--	906	6934	24858	32698

References

1. Bowles, J. S.; Mackenzie, J. K., The crystallography of martensite transformations I. Acta Metallurgica 1954, 2 (1), 129-137.

2. Mackenzie, J. K.; Bowles, J. S., The crystallography of martensite transformations II. Acta Metallurgica 1954, 2 (1), 138-147.

3. Wayman, C. M., The phenomenological theory of martensite crystallography: Interrelationships. Metallurgical and Materials Transactions A 1994, 25 (9), 1787-1795.

4. Krivy, I.; Gruber, B., A unified algorithm for determining the reduced (Niggli) cell. Acta Crystallographica Section A 1976, 32 (2), 297-298.

5. Gruber, B., The relationship between reduced cells in a general Bravais lattice. Acta Crystallographica Section A 1973, 29 (4), 433-440.

6. Grosse-Kunstleve, R. W.; Sauter, N. K.; Adams, P. D., Numerically stable algorithms for the computation of reduced unit cells. Acta Crystallographica Section A 2004, 60 (1), 1-6.

7. Andrews, L. C.; Bernstein, H. J.; Sauter, N. K., Selling reduction versus Niggli reduction for crystallographic lattices. Acta Crystallogr A Found Adv 2019, 75 (Pt 1), 115-120.

8. Pyykkö, P.; Atsumi, M., Molecular Single-Bond Covalent Radii for Elements 1–118. Chemistry – A European Journal 2009, 15 (1), 186-197.

9. Isayev, O.; Oses, C.; Toher, C.; Gossett, E.; Curtarolo, S.; Tropsha, A., Universal fragment descriptors for predicting properties of inorganic crystals. Nature Communications 2017, 8 (1), 15679.

10. Blatov *, V. A., Voronoi–dirichlet polyhedra in crystal chemistry: theory and applications. Crystallography Reviews 2004, 10 (4), 249-318.

11. Ford, L. R.; Fulkerson, D. R., Maximal Flow Through a Network. Canadian Journal of Mathematics 1956, 8, 399-404.

12. Witman, M.; Ling, S.; Boyd, P.; Barthel, S.; Haranczyk, M.; Slater, B.; Smit, B., Cutting Materials in Half: A Graph Theory Approach for Generating Crystal Surfaces and Its Prediction of 2D Zeolites. ACS Central Science 2018, 4 (2), 235-245.

13. Shang, C.; Liu, Z. P., Stochastic Surface Walking Method for Structure Prediction and Pathway Searching. J.Chem.Theory Comput 2013, 9 (3), 1838-1845.

14. Shang, C.; Zhang, X. J.; Liu, Z. P., Stochastic surface walking method for crystal structure and phase transition pathway prediction. Physical chemistry chemical physics : PCCP 2014, 16 (33), 17845-56.

15. Zhang, X. J.; Shang, C.; Liu, Z. P., From Atoms to Fullerene: Stochastic Surface Walking Solution for Automated Structure Prediction of Complex Material. J.Chem.Theory Comput 2013, 9 (7), 3252-3260.

16. Huang, S.-D.; Shang, C.; Kang, P.-L.; Liu, Z.-P., Atomic structure of boron resolved using machine learning and global sampling. Chem. Sci. 2018.

17. Huang, S.-D.; Shang, C.; Zhang, X.-J.; Liu, Z.-P., Material discovery by combining stochastic surface walking global optimization with a neural network. Chem. Sci. 2017, 8 (9), 6327-6337.

18. Kresse, G.; Furthmüller, J., Efficient iterative schemes for \textit{ab initio} total-energy calculations using a plane-wave basis set. Phys. Rev. B 1996, 54 (16), 11169-11186.

19. Huang, S.-D.; Shang, C.; Kang, P.-L.; Zhang, X.-J.; Liu, Z.-P., LASP: Fast global potential energy surface exploration. Wiley Interdisciplinary Reviews-Computational Molecular Science 2019, 9 (6).